*Sound & Vibration* 2026, 60(4), 4263.
doi: https://doi.org/10.59400/sv4263

Article

# Tower dynamic response analysis of wind turbines during primary frequency regulation

**Yingwei Wang[1], Aolin Song[2,*], Tingxiang Zhang[2], Yilin Du[2]**

[1] The School of Electrical Engineering, Shenyang University of Technology, Shenyang 110870, China
[2] The Northeast Branch of State Grid Corporation of China, Shenyang 110001, China
*** Corresponding author:** Aolin Song, 15183359037@163.com

**CITATION**

Wang Y, Song A, Zhang T, et al. Tower dynamic response analysis of wind turbines during primary frequency regulation. Sound & Vibration. 2026; 60(4): 4263. https://doi.org/10.59400/sv4263

**ARTICLE INFO**

Received: 13 April 2026
Revised: 8 May 2026
Accepted: 15 May 2026
Available online: 21 July 2026



**Abstract:** As wind turbines increasingly participate in Primary Frequency Regulation (PFR) to support grid frequency stability, the accompanying mechanical load variations pose a potential threat to structural reliability. However, the underlying aero-electro-mechanical coupling mechanisms by which PFR-induced power and torque fluctuations affect tower dynamics have not been fully clarified. This study develops a multidimensional analytical model of a wind turbine with PFR to reveal the transmission path from grid frequency deviations to generator torque variations and subsequently to tower side-to-side (SS) bending moments. Frequency-domain and time-domain analyses show that generator torque, rather than aerodynamic thrust, is the dominant excitation source for tower SS vibration during PFR. The results further indicate that this excitation is highly phase-sensitive: the amplification or suppression of tower vibration depends on the instantaneous phase alignment between the torque disturbance and the tower's natural sway cycle. Therefore, identical PFR commands may lead to substantially different structural responses when activated at different instants. The analytical conclusions are validated using high-fidelity FAST co-simulations under stochastic wind and grid-disturbance scenarios. Quantitative fatigue evaluation shows that uncoordinated PFR may increase the tower SS Damage Equivalent Load (DEL) by up to 600% in low-wind-speed regimes. These findings demonstrate that future wind turbine PFR controllers should incorporate phase-aware coordination strategies to reduce structural resonance and fatigue risks while maintaining effective grid frequency support.

**Keywords:** wind turbine; tower; primary frequency regulation; vibration of side-to-side bending moment

## 1. Introduction

Wind turbines can significantly enhance system frequency stability through primary frequency regulation, owing to their inherent rotational inertia and control flexibility [1–4]. While extensive research has focused on optimizing control parameters to enhance frequency support, systematic consideration of wind turbine fatigue loads remains limited [5,6]. With the continuous increase in wind turbine size, fatigue-induced failure rates have become a growing concern. Currently, analyses of how primary frequency regulation affects wind turbine fatigue loads focus primarily on shaft torsional vibrations and drivetrain loads [7,8]. However, a critical issue remains unaddressed: the impact of rapid active power fluctuations—introduced during primary frequency regulation—on the dynamic characteristics of the wind turbine tower.

As the key load-bearing structure of a wind turbine, the tower experiences fatigue damage that directly impacts its safe operational lifespan. Tower loads arise primarily from complex aerodynamic forces, gravitational loads, and dynamic responses during turbine operation [9]. Existing studies on frequency regulation loads have predominantly focused on drivetrain torsional vibrations, leaving tower loads largely unexamined. This imbalance stems from a widely held implicit assumption: because primary frequency regulation is executed via the generator torque channel, its impacts are confined to the electrical system and drivetrain, rendering its effect on the support structure negligible [10]. However, as wind turbines continue to scale up, the impact of primary frequency regulation on the support structure can no longer be overlooked. Rapid fluctuations in generator electromagnetic torque act not only on the drivetrain; the resulting reaction forces also propagate through the nacelle bedplate to the tower top, thereby exciting structural vibrations, particularly the tower's natural modes [11]. Driven by the ongoing upscaling of turbine capacities to 10 MW and beyond, the increased tower height and structural flexibility significantly lower the first natural frequency. This reduction makes the tower prone to overlapping with the primary energy distribution band of system frequency fluctuations. With the evolution of modern power systems, the sensitivity to low-frequency disturbances has intensified, shifting frequency fluctuation energy toward lower frequency bands [12]. The convergence of decreasing tower natural frequencies and intensifying system disturbances significantly elevates the risk of induced resonance and exacerbated fatigue, as dynamic generator torque excitation during primary frequency regulation increasingly impacts the tower structure.

While extensive research has focused on optimizing control strategies to enhance PFR, there is a growing consensus in recent studies that active participation in grid frequency support inevitably exacerbates the dynamic oscillation of fatigue loads across the wind turbine structure. Historically, the critical analysis of PFR-induced fatigue has predominantly concentrated on the drivetrain, revealing how inertial control generates severe torque fluctuations that shorten the service life of the main shaft. However, the transient impact of these rapid active power variations on the primary load-bearing component—the tower—has not been sufficiently evaluated.

Although advanced active control frameworks have proven effective in mitigating tower SS loads under conventional aerodynamic disturbances, their structural implications during the highly transient active power fluctuations specifically induced by PFR remain underexplored. Existing literature largely treats the frequency-induced load simply as a generic additive broadband disturbance, fundamentally failing to account for the complex dynamic interactions—particularly the critical phase dependency—between PFR-induced electromagnetic torque disturbances and the inherent rigid-flexible coupling oscillations of large-scale towers.

To address the aforementioned challenges, this study systematically investigates the impact of rapid active power fluctuations during PFR on the structural dynamics of wind turbine towers. The novel contributions of this work are highlighted as follows: This study analytically reveals the direct coupling path between the grid frequency deviation and the tower's side-to-side (SS) bending moment, demonstrating that generator torque fluctuations act as the dominant excitation source for lateral tower loads. Through combined frequency-domain and time-domain analyses, a distinct phase dependency between the PFR-induced torque disturbances and the tower's inherent oscillation was identified, quantitatively explaining how identical PFR commands can either significantly amplify or suppress SS vibration risks. By constructing frequency-sensitive band scenarios for future renewable-dominated grids, this study provides a forward-looking evaluation, highlighting the severely escalated risk of SS tower resonance for future large-scale, low-frequency wind turbines.

The remainder of this paper is organized as follows. Section 2 develops the coupled aerodynamic-mechanical-electrical dynamic model of the wind turbine and its PFR control logic. Section 3 constructs typical scenarios for future modern power systems to analyze the evolution of their frequency response characteristics and the resulting changes in the tower's excitation environment. Section 4 derives the small-signal analytical model to conduct frequency-domain analyses on key state variables, revealing the underlying resonance risks and phase sensitivities of the tower's lateral vibrations. Section 5 provides a comprehensive quantitative analysis of the tower's fore-aft (FA) and SS fatigue loads based on high-fidelity co-simulations under representative PFR scenarios. Section 6 presents the discussion. Finally, Section 7 summarizes the main conclusions of the study.

## 2. Wind turbine dynamics and its PFR model

### 2.1. Wind turbine dynamic model

The dynamic model of a wind turbine is fundamentally composed of aerodynamic, drivetrain, and generator subsystems. Accordingly, the aerodynamic torque ($T_{\mathrm{a}}$) and the tower FA bending moment ($M_{\mathrm{Tfa}}$) can be formulated as [13]:

$$T_{\mathrm{a}} = 0.5\rho\pi R^2 v^3 C_p/\omega_{\mathrm{r}}, \tag{1}$$

$$M_{\mathrm{Tfa}} = 0.5\rho\pi R^2 v^2 C_t H_{\mathrm{tower}}, \tag{2}$$

where $v$ is the wind speed (m/s), $\rho$ is the air density (kg/m$^3$), $R$ is the rotor radius (m), $C_{\mathrm{p}}$ is the power coefficient, $C_{\mathrm{t}}$ is the thrust coefficient, $H_{\mathrm{tower}}$ is the hub height of the wind turbine in meters, and $\omega_{\mathrm{r}}$ is the rotor speed (rad/s).

The drivetrain dynamics are represented by a two-mass lumped-parameter model governed by the differential equations in (3)–(5) [13]:

$$J_{\mathrm{g}}\dot{\omega}_{\mathrm{g}} = T_s/\eta_{\mathrm{g}} - T_{\mathrm{g}}, \tag{3}$$

$$J_{\mathrm{r}}\dot{\omega}_{\mathrm{r}} = T_{\mathrm{a}} - T_{\mathrm{s}}, \tag{4}$$

$$T_s = \left(\frac{K}{s} + B\right)\left(\omega_{\mathrm{r}} - \frac{\omega_{\mathrm{g}}}{\eta_{\mathrm{g}}}\right), \tag{5}$$

where $T_{\mathrm{s}}$ is the shaft torque (Nm), $K$ is the torsional stiffness (Nm/rad), $B$ is the torsional damping (Nm·s/rad), $J_{\mathrm{r}}$ and $J_{\mathrm{g}}$ are the rotor and generator moments of inertia (kg·m²), respectively, $\omega_{\mathrm{g}}$ is the generator speed (rad/s), $T_{\mathrm{g}}$ is the generator torque (Nm), and $\eta_{\mathrm{g}}$

is the gearbox ratio.

A simplified representation of the generator and converter control systems is given by Equations (6)–(9) [13]:

$$\omega_{\mathrm{f}} = \frac{1}{1+\tau_{\mathrm{f}}}\omega_{\mathrm{g}}, \tag{6}$$

$$T_{\mathrm{g}} = \frac{P_{\mathrm{ref}}}{\omega_{\mathrm{g}}}\frac{1}{1+\tau_{\mathrm{g}}s}, \tag{7}$$

$$P_{\mathrm{ref}} = T_{\mathrm{g\_ref}}\omega_{\mathrm{f}}, \tag{8}$$

$$P_{\mathrm{out}} = T_{\mathrm{g}}\omega_{\mathrm{g}}, \tag{9}$$

where $P_{\mathrm{out}}$ is the wind turbine output power (W), $P_{\mathrm{ref}}$ is the generator reference input power (W), $\tau_{\mathrm{g}}$ is the generator inertia constant (s), $\tau_{\mathrm{f}}$ is the speed filter time constant (s), $T_{\mathrm{g\_ref}}$ is the reference generator torque derived from the torque controller (Nm), and $\omega_{\mathrm{f}}$ is the filtered generator speed (rad/s).

## 2.2. PFR model of wind turbines

Wind turbines provide PFR by adjusting their torque references. **Figure 1** illustrates the overall block diagram integrating torque, pitch, and PFR control. A derating factor $\gamma$ shifts the operation off the maximum power point tracking (MPPT) curve to proactively secure active power reserves. Furthermore, the grid frequency deviation $\Delta f$(p.u.) is multiplied by the PFR gain to yield a supplementary torque reference increment.

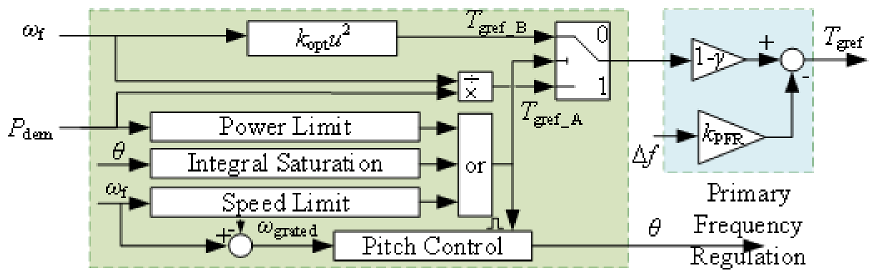


**Figure 1.** Block diagram of wind turbine inertia control.

Based on the control block diagram in **Figure 1**, the torque reference commands for primary frequency regulation under below-rated and above-rated wind speeds are given by Equations (10) and (11), respectively:

$$T_{\mathrm{gref\_B}} = (1-\gamma)k_{\mathrm{opt}}\omega_{\mathrm{f}}^2 - k_{\mathrm{PFRY}}\Delta f, \tag{10}$$

$$T_{\mathrm{gref\_A}} = (1-\gamma)P_{\mathrm{dem}}/\omega_{\mathrm{f}} - k_{\mathrm{PFRY}}\Delta f, \tag{11}$$

where $k_{\mathrm{opt}}$ is the optimal torque gain, configured to ensure a smooth and continuous transition of the generator torque reference ($T_{\mathrm{g\_ref0}}(\omega_{\mathrm{grated}}) = T_{\mathrm{g\_ref1}}(\omega_{\mathrm{grated}})$, where $\omega_{\mathrm{grated}}$ is the rated generator speed)); $P_{\mathrm{dem}}$ is the demanded power. $k_{\mathrm{PFRY}}$ is the dimensional primary frequency regulation gain (Nm/p.u.); and the subscripts "$_{\mathrm{\_B}}$" and "$_{\mathrm{\_A}}$" denote the below-rated and above-rated wind speed operating regions, respectively.

## 3. Analysis of frequency characteristics in new power systems

When a wind turbine participates in primary frequency regulation, the system frequency acts as a disturbance input. Consequently, analyzing the frequency response characteristics of modern power systems is a necessary first step. Accurately characterizing this frequency input is essential for elucidating its subsequent impact on tower loads.

### 3.1. Frequency scenario construction for new power systems

Drawing upon the projections [14, 15], **Figure 2** illustrates the forecasted trends in electricity generation across various energy sources within the power system from 2025 to 2060. Building upon these projections, we select representative scenarios at five-year intervals for detailed modeling and analysis. In the scenario construction, coal-fired and gas-fired power generation are aggregated into the category of thermal power. It is further specified that thermal and hydropower units consistently fulfill the system frequency regulation responsibilities.

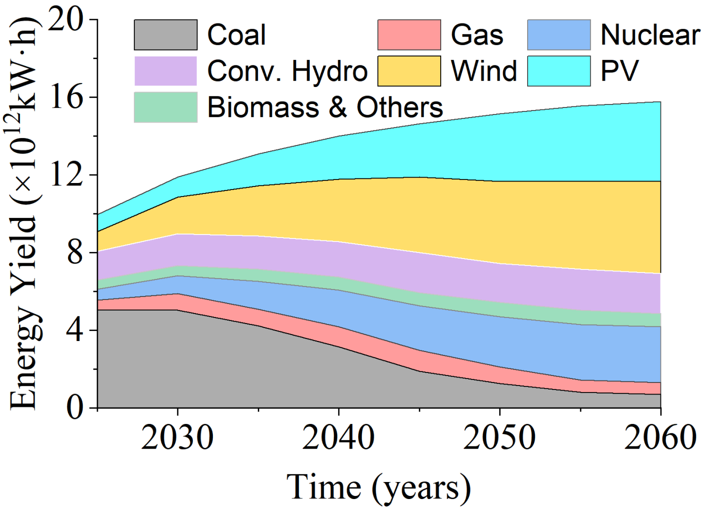


**Figure 2.** Forecast of power generation in power systems from different years.

### 3.2. Small-signal modeling of wind turbines by operating region

To analyze the impact of the wind turbine's participation in primary frequency regulation on the tower's dynamic response—particularly its load characteristics—we develop a small-signal model that captures the dynamic behavior of the unit. This model is derived by linearizing and per-unitizng the nonlinear dynamic model developed in Section 2 around a steady-state operating point. The detailed derivation is provided in **Appendix A**. Following this linearization procedure, the transfer functions relating the incremental power output of the wind turbine to the system frequency deviation input across different operating regions are derived as Equations (12) and (13):

$$G_W(s) = \frac{\mu_{87} + \frac{\mu_{38}\mu_{87}}{1-\frac{\mu_{34}\mu_{43}}{1-\frac{\mu_{42}\mu_{24}}{1-\mu_{21}\mu_{12}}}}}{1 - \frac{(\mu_{87}\mu_{65}\mu_{53}+\mu_{87}\mu_{53}+\mu_{83})\mu_{38}}{1-\frac{\mu_{34}\mu_{43}}{1-\frac{\mu_{42}\mu_{24}}{1-\mu_{21}\mu_{12}}}}}(sub-rated), \quad (12)$$

$$G_W(s)=\frac{\kappa_{87}+\frac{\kappa_{38}\kappa_{87}}{1-\frac{\kappa_{34}\left(\frac{\kappa_{42}\kappa_{21}\kappa_{19}\kappa_{95}\kappa_{53}}{1-\kappa_{21}\kappa_{12}}+\kappa_{43}\right)}{1-\frac{\kappa_{42}\kappa_{24}}{1-\kappa_{21}\kappa_{12}}}}}{1-\frac{(\kappa_{87}(\kappa_{65}\kappa_{53}+\kappa_{53})+\kappa_{83})\kappa_{38}}{1-\frac{\kappa_{34}\left(\frac{\kappa_{42}\kappa_{21}\kappa_{19}\kappa_{95}\kappa_{53}}{1-\kappa_{21}\kappa_{12}}+\kappa_{43}\right)}{1-\frac{\kappa_{42}\kappa_{24}}{1-\kappa_{21}\kappa_{12}}}}}(above-rated), \tag{13}$$

where, $\mu_{12}=\kappa_{12}=a_1, \mu_{21}=\kappa_{21}=\frac{a_4}{J_r s}, \kappa_{19}=a_3, \mu_{24}=\kappa_{24}=-\frac{a_5}{J_r s}, \mu_{34}=\kappa_{34}=\frac{a_6}{J_g s}, \mu_{38}=\kappa_{38}=-\frac{a_7}{J_g s}, \mu_{42}=\kappa_{42}=a_8\left(\frac{K_{\mathrm{Ts}}+B_{\mathrm{Ts}}s}{s}\right), \mu_{43}=\kappa_{43}=-a_9\left(\frac{K_{\mathrm{Ts}}+B_{\mathrm{Ts}}s}{s}\right)$, $\mu_{83}=\kappa_{83}=-\frac{1}{\tau_g s+1}$, $\mu_{53}=\kappa_{53}=\frac{1}{1+\tau_f s}$, $\kappa_{95}=b_1$, $\mu_{65}=a_{10}=\frac{2(1-\gamma)k_{\mathrm{opt}}\omega_{\mathrm{f0}}^2}{M_{\mathrm{gref0}}}$, $\kappa_{65}=a_{10}=-\frac{P_{\mathrm{dem0}}(1-\gamma)}{\omega_{\mathrm{f0}}M_{\mathrm{gref0}}}$, $\mu_{87}=\kappa_{87}=\frac{1}{\tau_g s+1}$. The aforementioned coefficients $a_i$ are detailed in **Appendix A**.

### 3.3. Analysis of frequency-sensitive bands in new power systems

In the context of the typical power system scenarios depicted in **Figure 2**, the closed-loop transfer function of the frequency deviation in response to a load disturbance is derived based on Cheng et al. [12], which yields Equation (14):

$$\frac{\Delta f(s)}{\Delta P_{\mathrm{L}}(s)}=\frac{1}{K_{\mathrm{T}}G_{\mathrm{T}}(s)+K_{\mathrm{H}}G_{\mathrm{H}}(s)-K_{\mathrm{W}}k_{\mathrm{PRE}}G_{\mathrm{W}}(s)-\frac{1}{G_{\mathrm{In}}(s)}}, \tag{14}$$

where $\Delta P_{\mathrm{L}}(s)$ is the load disturbance; $K_{\mathrm{T}}$, $K_{\mathrm{H}}$, and $K_{\mathrm{W}}$ denote the participation factors of thermal power, hydropower, and wind power, respectively, and the expressions for $G_{\mathrm{T}}(s)$ , $G_{\mathrm{H}}(s)$ and $G_{\mathrm{In}}(s)$ are detailed in **Appendix B**.

**Figures 3** and **4** illustrate the frequency response characteristics of the system subjected to load disturbances under two typical wind conditions: below-rated (average wind speed of 9 m/s) and above-rated (average wind speed of 15 m/s), respectively.

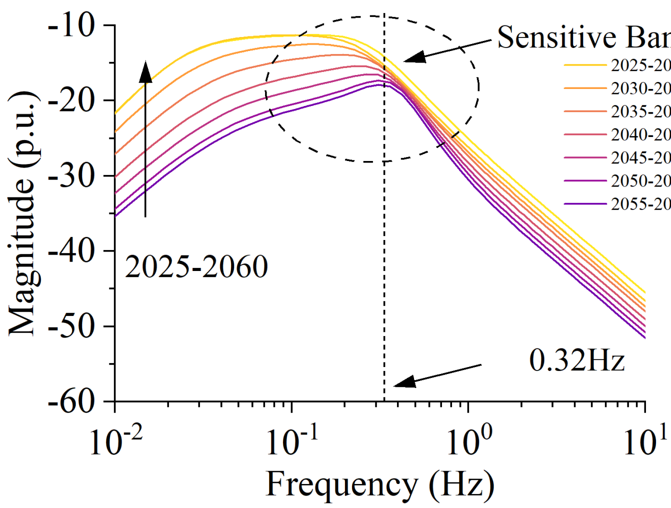


**Figure 3.** System frequency response to load disturbance below-rated wind speed.

In frequency-domain analysis, the magnitude response of the closed-loop transfer function characterizes the system's capability to attenuate load disturbances across various frequencies. A lower magnitude indicates a smaller frequency deviation induced by disturbances at that specific frequency, which corresponds to enhanced frequency stability. Drawing upon the concept of the frequency-sensitive band [16], this study primarily focuses on analyzing the system's behavioral characteristics in the vicinity of its frequency response magnitude peak. Driven by the evolution of modern power systems, the system's frequency-sensitive band has substantially broadened, expanding from the original 0.03–0.5 Hz to 0.01–0.5 Hz. Under below-rated wind conditions, the system's peak sensitive frequency in the 2025 scenario is approximately 0.32 Hz, and the magnitude at this peak consistently increases as the system evolves. Conversely, under above-rated conditions, the peak sensitive frequency is located at approximately 0.38 Hz. Within the aforementioned sensitive band, an overall increase in magnitude is observed, indicating a degradation in the system's capability to reject load disturbances. This signifies that the frequency deviation induced by load disturbances within this specific band will be substantially amplified, subsequently exacerbating the generator torque fluctuations.

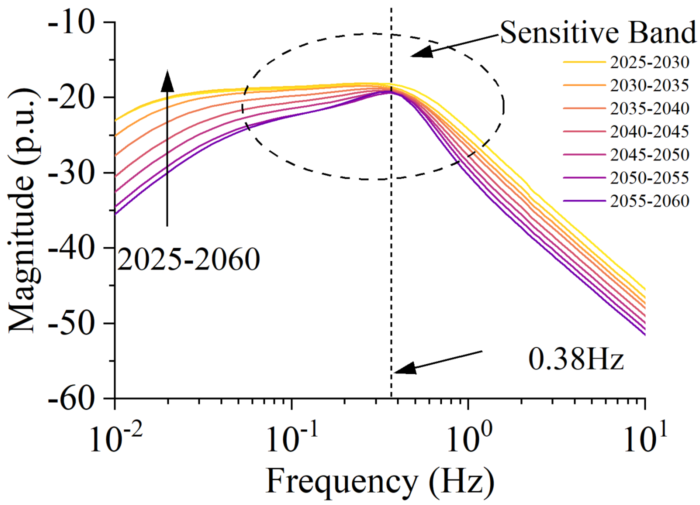


**Figure 4.** System frequency response to load disturbance above-rated wind speed.

For the NREL 5-MW wind turbine investigated in Jonkman et al. [17], the fundamental modal frequency of the tower is approximately 0.32 Hz. As the unit capacity continues to scale up, this first-order modal frequency of the tower structure exhibits a downward trend (detailed analysis is provided in subsequent sections). Given the close proximity of the tower's fundamental modal frequency to the system's frequency-sensitive band, the coupling between system frequency fluctuations and tower moments may induce severe tower-control system coupled vibrations. Consequently, how the power fluctuations within specific frequency bands—particularly below 0.4 Hz—introduced by primary frequency regulation excite tower resonance and exacerbate fatigue loads constitutes the core issue to be addressed in the subsequent sections.

## 4. The impact of PFR on tower loads

This section delves into the underlying mechanisms by which a wind turbine's participation in primary frequency regulation impacts its tower structural loads, with a primary focus on potential vibration risks.

## 4.1. Analytical modeling of tower load response

Based on the dynamic model of the wind turbine, the linearized expressions for the tower load components in response to system disturbances can be directly derived, as formulated in Equations (15) and (16) [8].

$$\Delta M_{\mathrm{Tfa}} = \frac{\partial M_{\mathrm{Tfa}}}{\partial \omega_{\mathrm{r}}}\Delta\omega_{\mathrm{r}} + \frac{\partial M_{\mathrm{Tfa}}}{\partial \theta}\Delta\theta + \frac{\partial M_{\mathrm{Tfa}}}{\partial v}\Delta v, \tag{15}$$

$$\Delta M_{\mathrm{Tss}} = \frac{\partial M_{\mathrm{Tss}}}{\partial a_{\mathrm{r}}}\Delta\omega_{\mathrm{r}} + \frac{\partial M_{\mathrm{Tss}}}{\partial \theta}\Delta\theta + \frac{\partial M_{\mathrm{Tss}}}{\partial T_{\mathrm{g}}}\Delta M_{\mathrm{g}} + \frac{\partial M_{\mathrm{Tss}}}{\partial v}\Delta v. \tag{16}$$

Equations (15) and (16) demonstrate that the tower's FA bending moment is primarily governed by the dynamic coupling among rotor speed, pitch angle, and wind speed, whereas the SS bending moment is directly coupled with the dynamic variations in generator torque. This distinction reveals a fundamental difference in the underlying mechanisms by which participation in primary frequency regulation impacts the FA and SS dynamic loads of the tower.

Given that the analytical model for the SS bending moment incorporates complex dynamic elements—such as multiple integrators—deriving an explicit transfer function is highly intractable. Consequently, a qualitative analysis is necessary. To this end, it is imperative to further establish the analytical relationship between the key state variables and the system frequency deviation. Building upon the wind turbine's small-signal model, the response functions mapping the critical state variables to the frequency deviation are derived as follows. These formulations serve to analyze the dynamic responses of individual subsystems under primary frequency regulation:

$$\frac{\Delta\omega_{\mathrm{r\_B}}(s)}{\Delta f(s)} = \frac{\mu_{24}}{1-\mu_{21}\mu_{12}}\frac{\mu_{43}}{1-\frac{\mu_{42}\mu_{24}}{1-\mu_{21}\mu_{12}}}\frac{\Delta\omega_{\mathrm{g\_B}}(s)}{\Delta f(s)}, \tag{17}$$

$$\frac{\Delta\omega_{\mathrm{r\_A}}(s)}{\Delta f(s)} = \frac{\kappa_{21}\kappa_{19}\kappa_{95}\kappa_{53}+\kappa_{24}\kappa_{43}}{1-(\kappa_{21}\kappa_{12}+\kappa_{24}\kappa_{42})}\frac{\Delta\omega_{\mathrm{g\_A}}(s)}{\Delta f(s)}, \tag{18}$$

$$\frac{\Delta\theta(s)}{\Delta f(s)} = \kappa_{95}\kappa_{53}\frac{\Delta\omega_{\mathrm{g\_A}}(s)}{\Delta f(s)}, \tag{19}$$

$$\frac{\Delta T_{\mathrm{g\_B}}(s)}{\Delta f(s)} = (\mu_{87}\mu_{65}\mu_{53}+\mu_{87}\mu_{53}+\mu_{83})\times\frac{\Delta\omega_{\mathrm{g\_B}}(s)}{\Delta f(s)} - k_{\mathrm{PFR}}\mu_{87}, \tag{20}$$

$$\frac{\Delta T_{\mathrm{g\_A}}(s)}{\Delta f(s)} = (\kappa_{87}\kappa_{65}\kappa_{53}+\kappa_{87}\kappa_{53}+\kappa_{83})\times\frac{\Delta\omega_{\mathrm{g\_A}}(s)}{\Delta f(s)} - k_{\mathrm{PFR}}\kappa_{87}, \tag{21}$$

where, $\frac{\Delta\omega_{\mathrm{g\_B}}(s)}{\Delta f(s)}$ and $\frac{\Delta\omega_{\mathrm{g\_A}}(s)}{\Delta f(s)}$ are detailed in **Appendix C**.

## 4.2. Frequency-domain analysis of key state variable dynamics

Based on Equations (17)–(21), the frequency response characteristics of each state variable in response to $\Delta f$ are analyzed using Bode plots. Consequently, the specific effects of these state variables on tower structural loads are derived to unveil the impact patterns of primary frequency regulation parameters and varying wind speeds.

Rotor speed response ($\Delta\omega_{\mathrm{r}}/\Delta f$): As illustrated in **Figures 5** and **6**, under below-rated wind conditions, an increase in wind speed or $\gamma$ attenuates the magnitude gain. Conversely, an elevated frequency regulation gain amplifies the magnitude of the rotor speed response. Above-rated wind conditions: The overall magnitude gain is comparatively lower than that in the below-rated regime. This signifies that primary frequency regulation exerts a less pronounced impact on the rotor speed in this operating region. Notably, the impact patterns of the parameters closely mirror those observed under below-rated conditions. As illustrated in **Figure A1** of **Appendix D**, under a 10% step load disturbance, the amplitude of rotor speed fluctuations induced by primary frequency regulation remains bounded within 5%. This directly corroborates the relative magnitude of the impact revealed by the frequency-domain analysis.

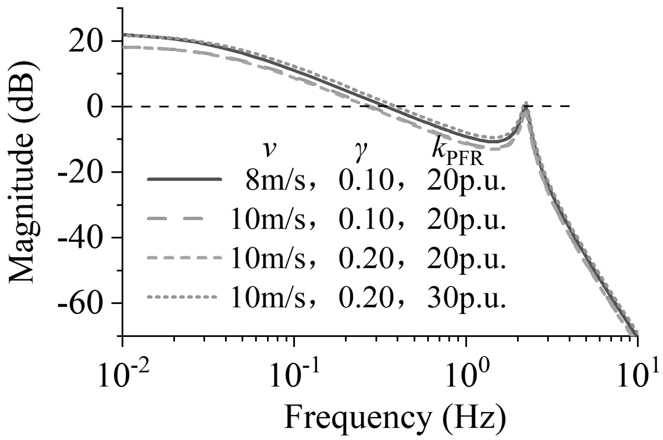


**Figure 5.** Bode plot of rotor speed response (below-rated wind speed).

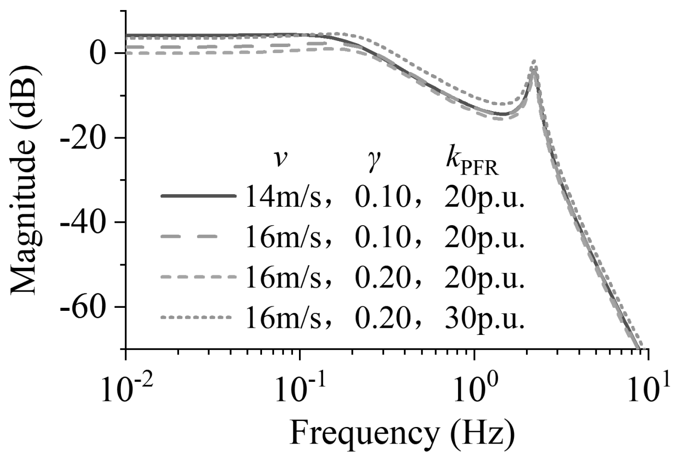


**Figure 6.** Bode plot of rotor speed response (above-rated wind speed).

Pitch angle response ($\Delta\beta/\Delta f$): As illustrated in **Figure 7**, an increase in wind speed or the de-rating factor attenuates the magnitude of the pitch angle response. Conversely, an elevated frequency regulation gain intensifies this impact, leading to a higher response amplitude. Since pitch control primarily plays an auxiliary role during primary frequency regulation, the resulting pitch angle variation remains limited. Specifically, a 10% step load disturbance leads to a pitch angle change of no more than 6% (refer to **Figure A2** in **Appendix D** for details).

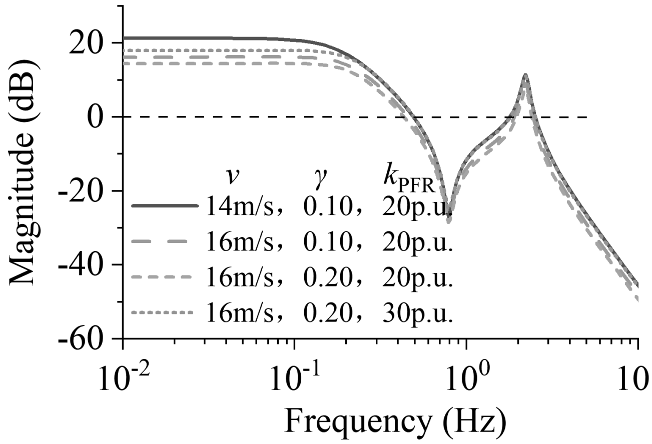


**Figure 7.** Bode plot of pitch angle response.

Generator torque response ($\Delta T_g/\Delta f$): As illustrated in **Figure 8**, under below-rated wind conditions, the magnitude gain remains substantially above zero across a broad frequency band of 0.01–10 Hz. This indicates that primary frequency regulation exerts a pronounced impact on the generator torque. An increase in wind speed or the de-rating factor attenuates the magnitude of its impact. Conversely, an elevated primary frequency regulation gain amplifies this influence. Above-rated wind conditions: As illustrated in **Figure 9**, the generator torque also exhibits high sensitivity to frequency deviations. Variations in wind speed and the de-rating factor have a relatively minimal impact on its frequency response characteristics, whereas an increase in the primary frequency regulation gain consistently enhances the response magnitude.

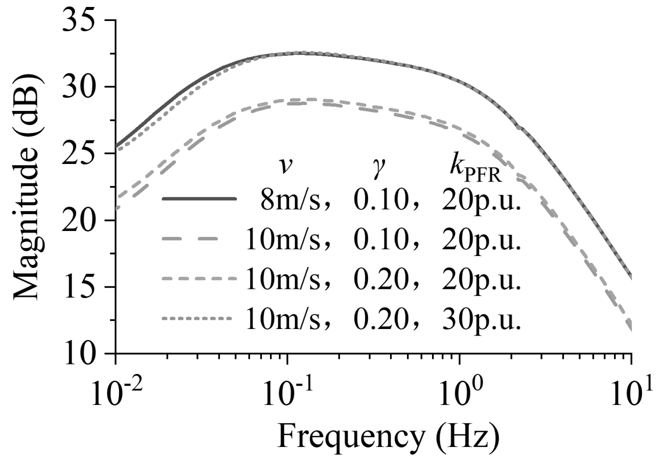


**Figure 8.** Bode plot of generator torque response (below-rated wind speed).

As illustrated in **Figure A3** of **Appendix D**, in response to primary frequency regulation, the generator torque is subjected to a significant impulsive load, rapidly reaching its peak value. Most critically, given the direct coupling between the tower's SS bending moment and the generator torque, the rapid torque fluctuations induced by primary frequency regulation pose a potential risk of exciting SS tower resonance. Consequently, the ensuing analysis will focus primarily on the tower's SS vibrations.

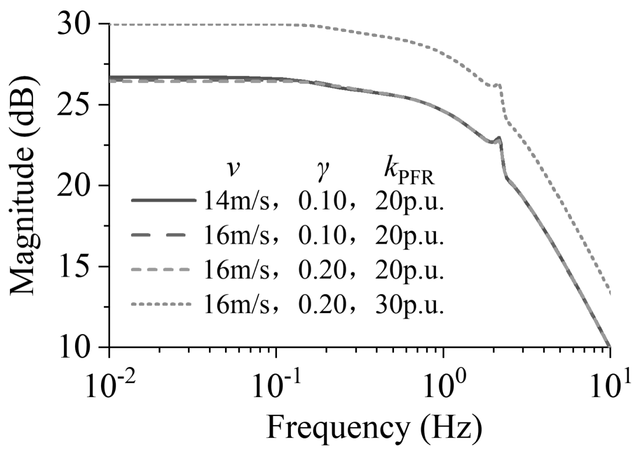


**Figure 9.** Bode plot of generator torque response (above-rated wind speed).

### 4.3. Analysis of tower vibration characteristics and resonance risk

As illustrated in **Figures 10** and **11**, the power spectral density (PSD) profiles of the generator torque exhibit both amplification and attenuation following the activation of frequency regulation. This indicates that primary frequency regulation may either exacerbate or suppress the torque excitation energy within the responsive frequency band.

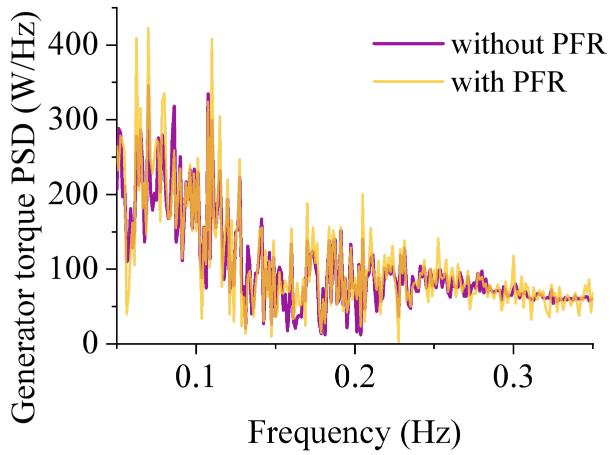


**Figure 10.** Power spectral density of generator torque (below-rated wind speed).

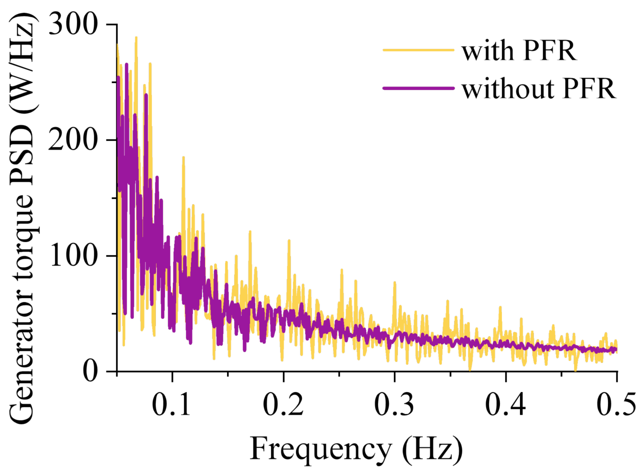


**Figure 11.** Power spectral density of generator torque (above-rated wind speed).

As illustrated in **Figures 12** and **13**, across varying wind conditions, participation in primary frequency regulation consistently induces an amplification in the PSD of the tower's SS bending moment in the vicinity of 0.32 Hz. This demonstrates that the dynamic generator torque fluctuations induced by primary frequency regulation—particularly within the critical frequency band—significantly exacerbate the tower's SS vibrations.

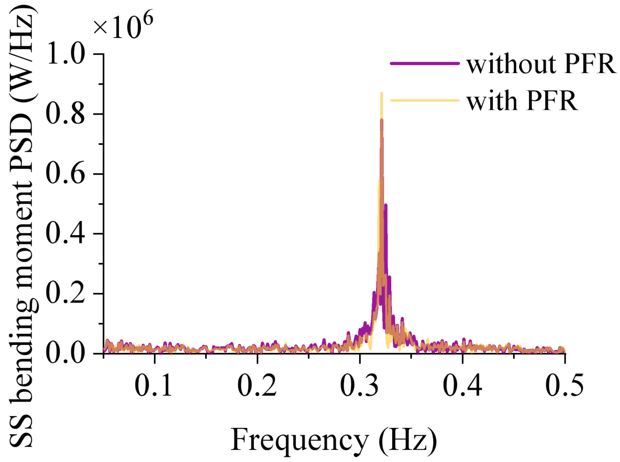


**Figure 12.** Power spectral density of tower side-to-side bending moment (below-rated wind speed).

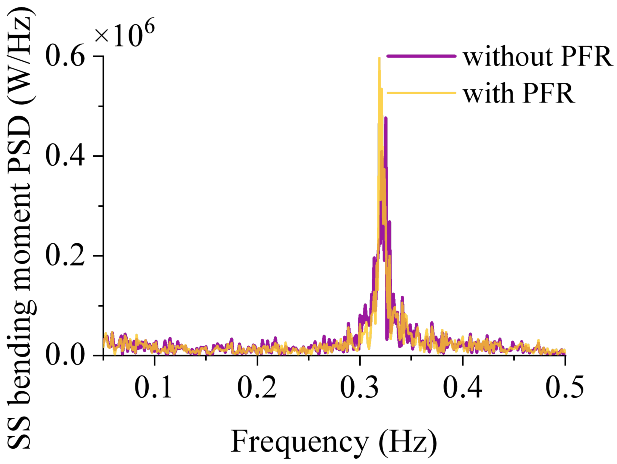


**Figure 13.** Power spectral density of tower side-to-side bending moment (above-rated wind speed).

Given that the power spectral density of the generator torque exhibits both amplification and attenuation in the vicinity of 0.32 Hz, determining whether primary frequency regulation ultimately exacerbates or suppresses the tower's SS fatigue loads necessitates a comprehensive analysis incorporating system disturbance characteristics and phase relationships.

Based on the clear spectral amplification depicted in **Figures 12** and **13**—where the PSD of the tower side-to-side bending moment with PFR (yellow lines) visibly dominates the baseline without PFR (purple lines) around the 0.32 Hz natural frequency—it can be definitively concluded that the implementation of PFR does not provide benefits in terms of the wind turbine's structural stability. On the contrary, it degrades the mechanical stability by amplifying the tower side-to-side resonance risks.

This observation highlights a critical operational trade-off in modern wind energy systems: while PFR is fundamentally designed to provide remarkable benefits for grid frequency stability (from an electrical power system perspective), it inadvertently compromises the structural stability of the individual wind turbine (from a mechanical perspective) by introducing additional broadband torque excitations (as evidenced by the high-frequency fluctuations in **Figures 10** and **11**). Therefore, acknowledging and mitigating this structural degradation while simultaneously fulfilling grid support requirements remains a key challenge for future PFR control design.

## 4.4. Analysis of phase sensitivity for lateral tower vibration

Both the generator torque and the tower's SS bending moment fluctuations act as vector quantities; thus, the instantaneous alignment of their dynamic interaction—whether in-phase or out-of-phase—plays a critical role. Based on the fundamentals of vector addition:

- When the fluctuation direction of $\Delta T_{\mathrm{g}}$ perfectly aligns with the inherent oscillation direction of $\Delta M_{\mathrm{Tss}}$ (i.e., an in-phase relationship), the tower's SS vibrations are significantly amplified.
- When the fluctuation direction of $\Delta T_{\mathrm{g}}$ is opposite to the inherent oscillation direction of $\Delta M_{\mathrm{Tss}}$ (i.e., an out-of-phase relationship), the tower's SS vibrations are effectively suppressed.

To verify this phase sensitivity, 10% step load disturbances applied at distinct initial instants (with 0.3 s intervals, equivalent to 3.33 Hz) were simulated under identical mean wind speeds. This specific interval was deliberately selected to sweep across various phase points within the inherent oscillation period (3.125 s, 0.32 Hz) of the tower's SS bending moment.

**Figures 14** and **15** illustrate the response trajectories of the generator torque and the corresponding tower SS bending moment under various initial instants, respectively. As highlighted by the bold orange and dark purple curves, the $\Delta T_{\mathrm{g}}$ fluctuations triggered at different instants lead to significantly distinct amplitude responses in $\Delta M_{\mathrm{Tss}}$. Specifically, the evaluation of **Figure 15** reveals a stark contrast: under the worst-case in-phase alignment (bold orange curve), the peak-to-peak fluctuation of the tower SS moment is drastically magnified, creating severe transient mechanical stress. Conversely, under the most favorable out-of-phase alignment (bold dark purple curve), the dynamic load is visibly dampened, maintaining a much narrower and flatter fluctuation band. This indicates that the transient structural load is highly deterministic and strictly governed by the timing of the PFR intervention.

**Figures 16** and **17** illustrate the evaluation results for the super-rated (above-rated) wind speed region. While the baseline tower SS moments exhibit different dynamic characteristics in this region due to higher aerodynamic thrust and active pitch control interventions, it is observed that the phase sensitivity phenomenon remains highly consistent with the observations made below the rated wind speed. A cross-evaluation between **Figures 15** and **17** indicates that, regardless of the operating wind speed regime, the injection of identical torque disturbances can either inherently aggravate or effectively alleviate the tower vibrations solely based on the initial phase condition.

Consequently, these response trajectories quantitatively confirm that modern PFR techniques must incorporate phase-aware or structure-conscious control logic. Blindly applying torque steps without considering the tower's instantaneous sway phase can lead to accidental resonance exacerbation during grid-support events.

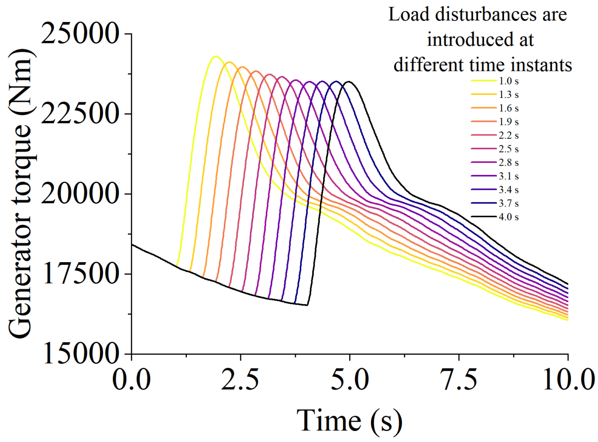


**Figure 14.** Generator torque response trajectories under different initial time conditions (below-rated wind speed).

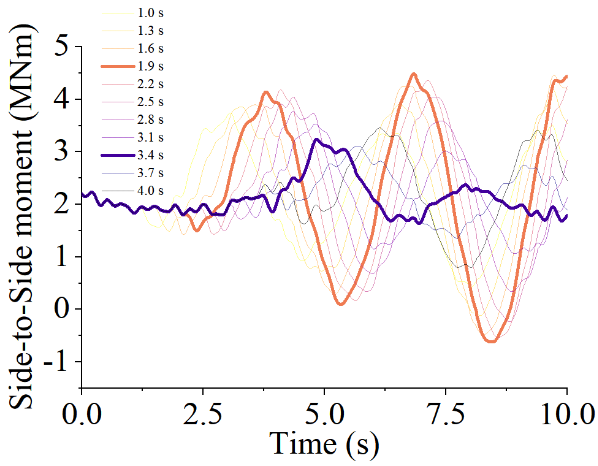


**Figure 15.** Tower side-to-side bending moment response trajectories under different initial time conditions (below-rated wind speed).

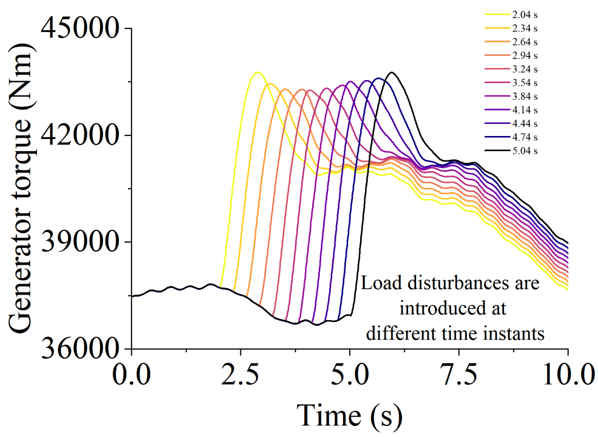


**Figure 16.** Generator torque response trajectories under different initial time conditions (above-rated wind speed).

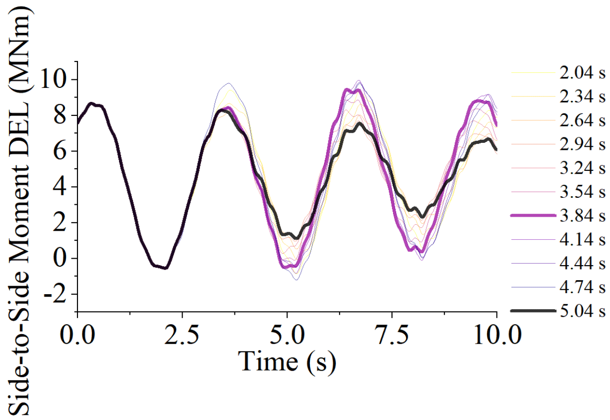


**Figure 17.** Tower side-to-side bending moment response trajectories under different initial time conditions (above-rated wind speed).

## 4.5. Tower vibration trend prediction

Typically, a wind turbine tower is idealized as a cantilever beam with a lumped mass at its top. As turbine units scale up in capacity, the significant increase in tower height $L$ inherently leads to a gradual reduction in the first-order natural frequency [18]. Studies indicate that the fundamental frequency of 10 MW-class turbine towers can drop to approximately 0.20 Hz [19], representing a significant reduction compared to the 0.32 Hz observed in the 5 MW turbine studied in this paper. Meanwhile, the PSD analysis of the system frequency reveals a significant upward trend in the low-frequency band near 0.2 Hz as the power system evolves. This implies that the low-frequency (0.2 Hz) components of frequency fluctuations will become increasingly pronounced in future new-type power systems.

When large-scale wind turbines participate in primary frequency regulation, the tower's natural frequency inevitably overlaps with the sensitive low-frequency bands where system frequency fluctuation energy is most concentrated. Such frequency coincidence—where the tower's natural frequency aligns with the dominant system disturbance frequencies—significantly escalates the risk of SS tower resonance.

In summary, the participation of wind turbines in primary frequency regulation, facilitated by the potent coupling between generator torque and tower SS bending moment, poses a significant risk of exacerbating lateral tower vibrations—a phenomenon that exhibits pronounced phase sensitivity. As wind turbines continue to scale up and new-type power systems evolve, the risk of SS tower resonance is poised to escalate significantly. The reduction in the tower's fundamental frequency heightens its susceptibility to inherent low-frequency system fluctuations, while the intensification of these low-frequency disturbances provides a more potent excitation source. In the design phase of large-scale wind turbines—particularly for towers and control systems—and the formulation of operational PFR algorithms, it is imperative to prioritize the low-frequency lateral vibrations and fatigue induced by grid frequency regulation. Developing intelligent PFR strategies with integrated vibration suppression or structural control measures is essential to ensuring the long-term structural integrity and reliability of the units.

## 5. Tower loads based on primary frequency regulation scenarios

The preceding sections, grounded in mechanistic modeling, have elucidated the potential impact mechanisms of wind turbine participation in PFR on tower loads, with a specific focus on SS loading. However, actual wind turbine operation is characterized by immense complexity, involving strong aero-servo-elastic coupling across multiple physical domains. To more accurately quantify the impact of PFR on tower fatigue loads, this section utilizes a high-fidelity simulation platform for a comprehensive numerical investigation.

The simulation is implemented using the industry-standard wind turbine aero-servo-elastic code, FAST v8, coupled with MATLAB/Simulink to establish a comprehensive mechanical-electrical co-simulation framework [20]. Within this framework, FAST governs the high-fidelity computations of aeroelastic and fatigue dynamics subjected to turbulent inflows, while MATLAB/Simulink facilitates the implementation of PFR control logic and the emulation of grid frequency disturbances. TurbSim is employed to generate stochastic turbulent wind fields that conform to the IEC 61400-1 standard [21]. For each combination of target mean wind speed and turbulence intensity, ten independent wind speed time series are generated to adequately characterize the stochastic nature of the wind resource. Considering the stochastic nature of system load variations, a stochastic load disturbance signal is adopted to serve as the excitation source for emulating frequency excursions in the power grid. Tower loads—specifically the resulting fatigue damage—are quantified via the Damage Equivalent Load (DEL) approach. The calculation of DEL is grounded in the Palmgren-Miner linear cumulative damage rule and the material-specific S-N curve, effectively characterizing the extent of fatigue damage under stochastic, variable-amplitude load spectra [22].

To isolate the impact of PFR while fully accounting for the dual stochasticity of wind inflows and load perturbations, the following multi-step simulation strategy is employed. First, for a fixed mean wind speed and turbulence intensity, ten independent TurbSim wind speed sequences are generated. Second, an identical stochastic load disturbance signal is applied across each wind sequence to emulate the grid frequency deviation ($\Delta f$). Third, comparative simulations are executed for scenarios both without PFR participation ($k_{\mathrm{PFR}} = 0$) and with PFR active. Subsequently, the Damage Equivalent Loads (DELs) for the tower FA and SS bending moments are computed for each individual run. Finally, to mitigate the influence of random variations, the DEL results from the ten simulation runs under the same wind condition are ensemble-averaged. This means serves as the representative value for the given scenario.

### 5.1. Complementarity between analytical and simulation approaches

It should be noted that the linearized analytical model developed in Sections 2–4 and the high-fidelity FAST co-simulation employed in this section serve complementary rather than redundant roles. The analytical model, derived via small-signal linearization around steady-state operating points, is specifically designed to reveal the fundamental coupling mechanisms—particularly the direct pathway from generator torque fluctuations to tower SS bending moments and the associated phase sensitivity. Its strength lies in providing physically transparent, closed-form insights that are not readily extractable from time-domain numerical simulations alone.

However, the linearized framework inherently introduces simplifications that limit its quantitative accuracy under realistic operating conditions. The principal factors contributing to deviations between the analytical predictions and the high-fidelity results are as follows:

(1) Linearization-induced limitations: The analytical model is linearized at a single operating point for each wind speed. During PFR events, the turbine undergoes transient excursions in rotor speed and generator torque that may extend beyond the small-signal validity range [23], causing the actual aerodynamic coefficients to deviate from their linearized approximations. This effect is particularly pronounced in the low wind speed regime, where the operating point sensitivity is highest—consistent with the observation in Subsection 5.2 that the most dramatic SS DEL increases (up to 600%) occur precisely in this region.

(2) Turbulent wind field complexity: The analytical model assumes a deterministic, uniform wind input, whereas the FAST simulations incorporate three-dimensional stochastic turbulent inflows generated by TurbSim in accordance with IEC 61400-1. Spatially coherent turbulence introduces additional broadband excitation—including tower shadow and wind shear effects—that modulates the generator torque spectrum in ways not captured by the single-input analytical framework [24].

(3) Structural coupling effects: The analytical model treats the tower SS dynamics in a decoupled manner, whereas FAST employs a multi-body elastic formulation that captures cross-coupling between the tower's FA and SS modes, as well as blade-tower interaction effects under large deflections.

These factors explain why the high-fidelity simulation is indispensable for quantitative fatigue assessment (Section 5), while the analytical model remains essential for mechanistic interpretation (Section 4) [25]. The two approaches are therefore employed in a sequential and complementary manner: the analytical model identifies what drives the tower SS response and why it is phase-sensitive, while the FAST simulation quantifies how much fatigue damage results under realistic stochastic conditions. This is consistent with fatigue-aware wind turbine inertial-control studies [26].

### 5.2. Quantitative analysis of tower axial loads

**Figure 18** illustrates the tower FA DEL under varying conditions. A comparison of the surfaces for different $k_{\mathrm{PFR}}$ values reveals that their morphologies are highly congruent, indicating that the participation of wind turbines in primary frequency regulation has a limited impact on tower FA fatigue loads within the investigated parameter range. These observations substantiate the conclusion that PFR exerts a marginal influence on FA fatigue loading.

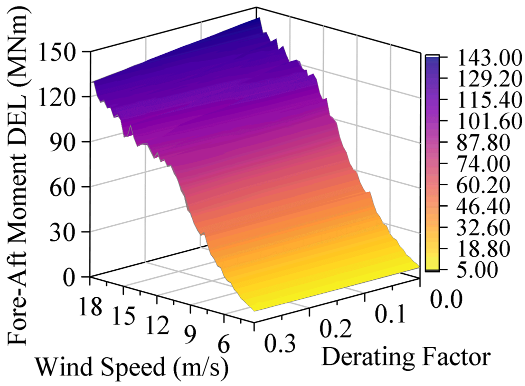


**Figure 18.** The DELs of tower fore-aft bending moment.

## 5.3. Quantitative analysis of tower lateral loads

The tower SS DEL results are presented in **Figure 19**. In stark contrast to the FA loading, PFR participation markedly affects the tower SS fatigue loads; notably, the tower exhibits a much higher susceptibility to these loads within the low wind speed range.

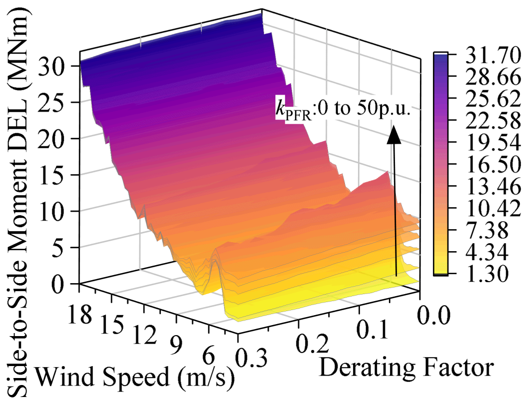


**Figure 19.** The DELs of tower side-to-side bending moment.

As illustrated in **Figures 20** and **21**, the tower SS DEL exhibits a substantial escalation in the low wind speed regime, peaking at a staggering 600% of the baseline value. This increment gradually diminishes as the wind speed increases. In the super-rated wind speed region, the variation in tower SS fatigue loads ranges from −5% to within 15%. Although occasional reductions are observed, the overall trend is still predominantly characterized by an increase.

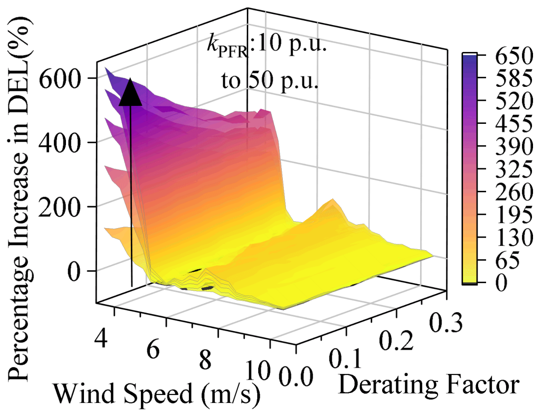


**Figure 20.** Rate of change of tower side-to-side DEL (below-rated wind speed).

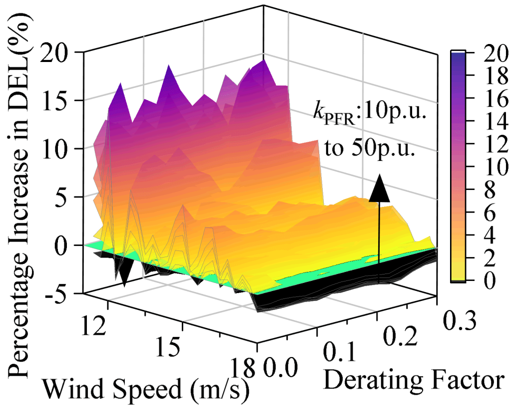


**Figure 21.** Rate of change of tower side-to-side DEL (above-rated wind speed).

## 6. Discussion

### 6.1. Synthesis of analytical and numerical findings

The results presented in Sections 4 and 5 provide two complementary perspectives on the impact of PFR on tower loads. The analytical model (Section 4) reveals the fundamental coupling mechanisms and identifies the generator torque as the dominant excitation pathway for tower SS vibrations. The high-fidelity FAST simulations (Section 5) subsequently quantify the resulting fatigue damage under realistic stochastic conditions. As summarized in **Table 1**, the key findings from both approaches are mutually consistent: both confirm the negligible impact of PFR on FA loads, the strong sensitivity of SS loads to PFR, and the critical role of the wind speed regime in determining the severity of structural penalties.

**Table 1.** Comparison of key findings from different methods.

| Aspect | Analytical prediction (Section 4) | FAST simulation (Section 5) |
|---|---|---|
| FA loads | Weakly coupled to $T_g$; governed by $\omega_r$, $\theta$, $v$ | DEL variation < 5% across all $k_{PFR}$ |
| SS loads | Directly coupled to $\Delta T_g$; resonance risk at 0.32 Hz | DEL increase up to 600% in low wind speeds |
| Phase sensitivity | In-phase amplification; out-of-phase suppression | Confirmed via multi-instant step simulations |
| Wind speed dependence | Higher magnitude gain at low wind speeds | Monotonically decreasing DEL sensitivity with increasing wind speed |

However, a quantitative gap inevitably exists between the linearized analytical predictions and the high-fidelity simulation results. This gap originates primarily from three factors: (1) the analytical model is linearized at a single operating point, whereas PFR events involve transient excursions that may exceed the small-signal validity range—particularly in the low wind speed regime where operating point sensitivity is highest; (2) the FAST simulations incorporate three-dimensional stochastic turbulence (wind shear, tower shadow, spatial coherence) that introduces broadband excitations not represented in the single-input analytical framework; and (3) the multi-body elastic formulation in FAST captures cross-coupling between FA and SS modes under large deflections, which is simplified in the analytical derivation. Despite these differences, the two approaches serve complementary roles: the analytical model identifies what drives the tower SS response and why it is phase-sensitive, while the FAST simulation quantifies how much fatigue damage results under realistic conditions.

## 6.2. Implications for grid stability versus structural integrity

PFR is fundamentally designed to enhance the former by modulating generator torque in response to frequency deviations. However, as demonstrated by the spectral amplification in **Figures 12** and **13**—where the PSD of the tower SS bending moment increases significantly around 0.32 Hz when PFR is activated—this grid-level benefit is achieved at the cost of increased structural loading on the individual turbine. This trade-off is particularly severe in the sub-rated wind speed region, where the baseline aerodynamic damping of the SS mode is inherently low, and where PFR gain requirements (as mandated by grid codes) remain unchanged despite the turbine operating far from its rated capacity. Consequently, the structural penalty per unit of frequency support provided is disproportionately high in this regime.

This finding has direct implications for grid code design: future regulations should consider wind-speed-dependent PFR gain scheduling, whereby the frequency support contribution of individual turbines is modulated according to their instantaneous structural vulnerability. Such an approach would maintain aggregate grid support from wind farms while redistributing the structural burden away from the most vulnerable operating conditions.

## 6.3. Physical interpretation of phase sensitivity

The phase sensitivity phenomenon demonstrated in **Figures 14–17** warrants further physical interpretation. The tower SS mode, once excited, behaves as a lightly damped oscillator at 0.32 Hz. When a PFR-induced torque perturbation arrives at an instant that coincides with the peak velocity of the existing SS oscillation (i.e., zero displacement, maximum kinetic energy), the injected energy is maximally absorbed by the mode, leading to resonance amplification. Conversely, when the perturbation arrives at the instant of peak displacement (i.e., zero velocity, maximum potential energy), it acts against the restoring force and effectively extracts energy from the mode, resulting in vibration suppression. This interpretation is analogous to the well-known phenomenon of parametric excitation timing in structural dynamics.

From a practical standpoint, this phase dependency implies that if the tower's instantaneous SS vibration state could be monitored in real time (e.g., via accelerometers or strain gauges at the tower base), the PFR controller could strategically time its torque interventions to avoid—or even actively exploit—the phase relationship. Specifically, delaying or advancing the torque response by a fraction of the SS oscillation period could transform a potentially destructive resonance event into a beneficial damping action. This concept forms the basis for future "phase-aware" or "structurally-conscious" PFR control strategies.

## 6.4. Scalability concerns for future large-scale turbines

The trend analysis presented in Subsection 4.5 indicates that as turbine capacity increases beyond 10 MW, the tower's first natural frequency may decrease to approximately 0.20 Hz. Simultaneously, the evolution of renewable-dominated power systems shifts frequency fluctuation energy toward lower bands, as evidenced by the broadening of the system's frequency-sensitive band from 0.03–0.5 Hz to 0.01–0.5 Hz

(**Figures 3** and **4**). This convergence creates an increasingly hazardous overlap between the tower's modal frequency and the dominant system disturbance frequencies.

For the 5 MW turbine studied herein, the tower natural frequency already lies within the system's sensitive band. For future 10–15 MW turbines with natural frequencies near 0.20 Hz, this overlap will be even more pronounced, as 0.20 Hz falls squarely within the region of maximum spectral amplification observed in the 2,040–2,060 scenarios (**Figures 3** and **4**). This suggests that the SS fatigue penalty associated with PFR may escalate further for next-generation turbines unless proactive mitigation measures are incorporated at the design stage.

## 7. Conclusion

This study investigated the dynamic response of wind turbine towers during PFR, with particular emphasis on the SS bending moment induced by generator torque fluctuations. A coupled aerodynamic–mechanical–electrical analytical framework was developed to clarify the transmission mechanism from PFR-induced torque variations to tower structural responses. The frequency-domain analysis demonstrated that generator torque fluctuations acted as a dominant excitation source for tower SS vibration, especially when the excitation components approached the tower natural frequency of approximately 0.32 Hz. High-fidelity FAST simulations further confirmed that the activation of PFR amplified the power spectral density of the tower SS bending moment near this critical frequency under both below-rated and above-rated wind speed conditions. Therefore, although PFR is beneficial for grid frequency stability, it may degrade the structural stability of individual wind turbines by increasing tower resonance and fatigue risks. In addition, the time-domain response analysis revealed a clear phase sensitivity: torque disturbances introduced in phase with the inherent tower oscillation significantly amplified SS bending moment fluctuations, whereas out-of-phase disturbances could partially suppress the vibration response.

Future work should focus on developing structurally aware PFR control strategies that balance grid-support performance and turbine load mitigation. In particular, phase-aware torque control, notch-filter-based frequency shaping, or load-constrained PFR optimization could be introduced to reduce torque excitation near the tower natural frequency. Moreover, the present analytical model can be further improved by incorporating stochastic turbulent wind disturbances, operating-point-dependent aerodynamic coefficients, and nonlinear aero-servo-elastic coupling effects. These improvements would enable more accurate prediction of tower fatigue loads under realistic operating conditions and support the design of PFR strategies that are both grid-friendly and structure-friendly.

**Author contributions:** Conceptualization, YW; methodology, YW; software, YW; validation, YW, AS, TZ, and YD; formal analysis, YW; investigation, YW; resources, YW; data curation, AS; writing—original draft preparation, AS; writing—review and editing, AS; visualization, AS; supervision, YW; project administration, TZ and YD; funding acquisition, TZ and YD. All authors have read and agreed to the published version of the manuscript.

**Funding:** This research was funded by the Natural Science Foundation of Liaoning Province General Program, grant number 2025-MS-121, and the Qingdao Major Science and Technology Special Project, grant number 25-1-1-gjgg-4-gx.

**Institutional review board statement:** Not applicable.

**Informed consent statement:** Not applicable.

**Data availability statement:** The data that support the findings of this study are available from the corresponding author upon reasonable request.

**Acknowledgment:** The authors would like to thank Prof. Yufeng Guo of Harbin Institute of Technology for his technical guidance.

**Conflict of interest:** The authors declare no conflict of interest.

**AI use statement:** During the preparation of this work, the authors used Google Gemini for translation, language editing, proofreading, and formatting assistance only. The authors subsequently reviewed and edited the content as necessary and take full responsibility for the final content of the published article.

## References

1. Alutaybi A, Hamrouni C. Impact of vibration on wind turbine efficiency and LSTM-based power conversion prediction. Sound & Vibration. 2025; 59(3): 2059. doi: 10.59400/sv2059
2. Kumar K, Prabhakar P, Verma A. Wind power forecasting technologies: A review. Energy Storage and Conversion. 2024; 2(2): 538. doi: 10.59400/esc.v2i2.538
3. Li L, Zhu D, Zou X, et al. Review of frequency regulation requirements for wind power plants in international grid codes. Renewable and Sustainable Energy Reviews. 2023; 187: 113731. doi: 10.1016/j.rser.2023.113731
4. He C, Geng H, Rajashekara K, et al. Analysis and Control of Frequency Stability in Low-Inertia Power Systems: A Review. IEEE/CAA Journal of Automatica Sinica. 2024; 11(12): 2363–2383. doi: 10.1109/JAS.2024.125013
5. Wang H, Yang Z, Chen Z, et al. Multiple Adaptive Model Predictive Controllers for Frequency Regulation in Wind Farms. IEEE Transactions on Energy Conversion. 2023; 38(1): 15–26. doi: 10.1109/TEC.2022.3210176
6. Huang Z, Yang X, Hu S, et al. An Optimal Active Power Allocation Method for Wind Farms Considering Unit Fatigue Load. Sustainability. 2025; 17(20): 9189. doi: 10.3390/su17209189
7. Tavares TM, Giesbrecht M. Deep Learning-Based Fault Diagnosis in Wind Turbine Bearings and Gearboxes Using Vibration Signals: Survey, Challenges, and Recommendations. IEEE Access. 2025; 13: 207013–207032. doi: 10.1109/ACCESS.2025.3636831
8. Wang Y, Guo Y, Xu W. Impact mechanism of frequency response on wind turbine fatigue load. Journal of Renewable and Sustainable Energy. 2023; 15(3): 033304. doi: 10.1063/5.0132363
9. Zhang M, Xie C, Li T, et al. Wind-Induced Response Analysis and Fatigue Life Prediction of a Hybrid Wind Turbine Tower Combining an Upper Steel Tube with a Lower Steel Truss. Buildings. 2024; 14(5): 1441. doi: 10.3390/buildings14051441
10. Wang D, Guo Y, Huang Y, et al. Torsional Vibration Analysis of Virtual-Synchronous-Controlled DFIG-Based Wind Turbines. IEEE Transactions on Sustainable Energy. 2025; 16(3): 2044–2057. doi: 10.1109/TSTE.2025.3544247
11. Lara M, Vázquez F, Sandua-Fernández I, et al. Adaptive Active Generator Torque Controller Design Using Multi-Objective Optimization for Tower Lateral Load Reduction in Monopile Offshore Wind Turbines. IEEE Access. 2023; 11: 115894–115910. doi: 10.1109/ACCESS.2023.3325840
12. Cheng Y, Azizipanah-Abarghooee R, Azizi S, et al. Smart frequency control in low inertia energy systems based on frequency response techniques: A review. Applied Energy. 2020; 279: 115798. doi: 10.1016/j.apenergy.2020.115798
13. Zhao H, Wu Q, Huang S, et al. Fatigue Load Sensitivity-Based Optimal Active Power Dispatch For Wind Farms. IEEE Transactions on Sustainable Energy. 2017; 8(3): 1247–1259. doi: 10.1109/TSTE.2017.2673122

14. Liu L, Wang Y, Wang Z, et al. Potential contributions of wind and solar power to China's carbon neutrality. Resources, Conservation and Recycling. 2022; 180: 106155. doi: 10.1016/j.resconrec.2022.106155
15. Ma Y, Li YP, Huang GH. Planning China's non-deterministic energy system (2021–2060) to achieve carbon neutrality. Applied Energy. 2023; 334: 120673. doi: 10.1016/j.apenergy.2023.120673
16. Lyu X, Groß D. Grid Forming Fast Frequency Response for PMSG-Based Wind Turbines. IEEE Transactions on Sustainable Energy. 2024; 15(1): 23–38. doi: 10.1109/TSTE.2023.3263858
17. Jonkman J, Butterfield S, Musial W, et al. Definition of a 5-MW Reference Wind Turbine for Offshore System Development (No. NREL/TP-500-38060, 947422). National Renewable Energy Laboratory; 2009. doi: 10.2172/947422
18. Wang S, Larsen TJ, Bredmose H. Ultimate load analysis of a 10 MW offshore monopile wind turbine incorporating fully nonlinear irregular wave kinematics. Marine Structures. 2021; 76: 102922. doi: 10.1016/j.marstruc.2020.102922
19. Wang L, Wang L, Hong Y. Mitigation of side-to-side vibration of a 10MW monopile offshore wind turbine under misaligned wind and wave conditions by an active torque control. Journal of Sound and Vibration. 2024; 574: 118225. doi: 10.1016/j.jsv.2023.118225
20. Wang X, Gao W, Scholbrock A, et al. Evaluation of different inertial control methods for variable-speed wind turbines simulated by fatigue, aerodynamic, structures and turbulence (FAST). IET Renewable Power Generation. 2017; 11(12): 1534–1544. doi: 10.1049/iet-rpg.2017.0123
21. Jonkman BJ, Buhl ML. TurbSim User's Guide (No. NREL/TP-500-36970, 15020326). National Renewable Energy Laboratory; 2005. doi: 10.2172/15020326
22. Buhl M. MCrunch User's Guide for Version 1.00. National Renewable Energy Laboratory; 2008. Available online: https://docs.nlr.gov/docs/fy08osti/43139.pdf
23. Cui R, Wang H, Liu Y, et al. VSG Frequency Response Strategy for Doubly-Fed Wind Farm Considering the Fatigue Load. Electronics. 2024; 13(12): 2310. doi: 10.3390/electronics13122310
24. Gasparis G, Lio WH, Meng F. Surrogate Models for Wind Turbine Electrical Power and Fatigue Loads in Wind Farm. Energies. 2020; 13(23): 6360. doi: 10.3390/en13236360
25. Yan W, Wang X, Gao W, et al. Electro-mechanical Modeling of Wind Turbine and Energy Storage Systems with Enhanced Inertial Response. Journal of Modern Power Systems and Clean Energy. 2020; 8(5): 820–830. doi: 10.35833/MPCE.2020.000272
26. Wang H, Liu Y, Wang X, et al. Dynamic synthetic inertial control method of wind turbines considering fatigue load. Frontiers in Energy Research. 2023; 10: 1067896. doi: 10.3389/fenrg.2022.1067896


# Appendix A

## Appendix A.1. Below the rated wind speed

For constant pitch operation below the rated wind speed, linearization of Equation (1) yields:

$$\delta T_{\mathrm{a}} = \frac{\partial T_{\mathrm{a}}}{\partial \omega_{\mathrm{r}}}\delta\omega_{\mathrm{r}} + \frac{\partial T_{\mathrm{a}}}{\partial v}\delta v, \tag{A1}$$

$$\frac{\delta T_{\mathrm{a}}}{T_{\mathrm{a0}}} = \frac{0.5\rho\pi R^2}{T_{\mathrm{a0}}}\left(\left(-\frac{v_0^3 C_{\mathrm{P0}}\omega_{\mathrm{r0}}}{\omega_{\mathrm{r0}}^2} + \frac{\omega_{\mathrm{r0}} v_0^2 R}{\omega_{\mathrm{r0}}}\frac{\partial C_{\mathrm{P0}}}{\partial\lambda}\right)\frac{\delta\omega_{\mathrm{r}}}{\omega_{\mathrm{r0}}} + \left(\frac{3v_0^3 C_{\mathrm{P0}} - v_0^2 R\omega_{\mathrm{r0}}}{\omega_{\mathrm{r0}}}\right)\frac{\delta v}{v_0}\right). \tag{A2}$$

The subscript labeled "0" denotes the stable operating point under current wind speed and derating factor conditions. Let: $\Delta T_{\mathrm{a}} = \delta T_{\mathrm{a}}/T_{\mathrm{a0}}$, $\Delta\omega_{\mathrm{r}} = \delta\omega_{\mathrm{r}}/\omega_{\mathrm{r0}}$, $\Delta v = \delta v/v_0$, the aerodynamic torque small-signal model can be derived as follows:

$$\Delta T_{\mathrm{a}}(s) = a_1\Delta\omega_{\mathrm{r}}(s) + a_2\Delta v(s). \tag{A3}$$

Among them, $a_1 = \frac{\omega_{\mathrm{r0}}}{v_0^3 C_{\mathrm{P0}}}\left(-\frac{v_0^3 C_{\mathrm{P0}}}{\omega_{\mathrm{r0}}} + v_0^2 R\frac{\partial C_{\mathrm{P0}}}{\partial\lambda}\right)$, $a_2 = \frac{3v_0 C_{\mathrm{P0}} - R\omega_{\mathrm{r0}}}{v_0 C_{\mathrm{P0}}}$.

Perform unitarization on Equations (3)–(5):

$$\Delta\omega_r(s) = \frac{1}{J_r s}\left(\alpha_4\Delta T_a(s) - \alpha_5\Delta T_s(s)\right), \tag{A4}$$

$$\Delta\omega_{\rm g}(s)=\frac{1}{J_{\rm g}s}\left(a_6\Delta T_s(s)-a_7\Delta T_{\rm g}(s)\right), \tag{A5}$$

$$\Delta T_s(s)=\frac{K_{\rm Ts}+B_{\rm Ts}s}{s}\left(a_8\Delta\omega_{\rm f}(s)-a_9\Delta\omega_{\rm g}(s)\right). \tag{A6}$$

Among them, $a_4=T_{\rm a0}/\omega_{\rm r0}$, $a_5=T_{\rm s0}/\omega_{\rm r0}$, $a_6=T_{\rm s0}/\left(\eta_{\rm g}\omega_{\rm g0}\right)$, $a_7=T_{\rm g0}/\omega_{\rm g0}$, $a_8=\omega_{r0}/\,T_{\rm s0}$, $a_9=\omega_{\rm g0}/\left(T_{\rm s0}\eta_{\rm g}\right)$.

Equation (8) is normalized as follows:

$$\Delta\omega_{\rm f}(s)=\frac{1}{1+\tau_{\rm f}s}\Delta\omega_{\rm g}(s). \tag{A7}$$

Equation (9) is normalized as follows:

$$\Delta T_{\rm gref}(s)=a_{10}\Delta\omega_{\rm f}(s)-a_{11}\Delta f(s). \tag{A8}$$

Among them, $a_{10}=2(1-\gamma)k_{\rm opt}\omega_{\rm f0}^2/T_{\rm gref0}$, $a_{11}=k_{\rm PFRY}/T_{\rm gref0}$, $a_{11}=k_{\rm PFKY}/T_{\rm grefN}$, $T_{\rm grefN}$ is the reference value for generator torque under re-rated operating conditions.

Unitarization of Equation (7):

$$\Delta P_{\rm ref}(s)=\Delta T_{\rm gref}(s)+\Delta\omega_{\rm f}(s). \tag{A9}$$

Substitute Equation (8) into the above equation:

$$\Delta P_{\rm ref}(s)=(1+a_{10})\,\Delta\omega_{\rm f}(s)-k_{\rm PFR}\Delta f(s). \tag{A10}$$

Unitarization of Equations (6) and (5):

$$\Delta T_{\rm g}(s)=\left(\Delta P_{\rm ref}(s)-\Delta\omega_{\rm g}(s)\right)\frac{1}{\tau_{\rm g}s+1}, \tag{A11}$$

$$\Delta P_{\rm Wout}(s)=\Delta T_{\rm g}(s)+\Delta\omega_{\rm g}(s). \tag{A12}$$

## Appendix A.2. Above the rated wind speed

Unitarization of Equation (1):

$$\Delta T_{\rm a}(s)=a_1\Delta\omega_{\rm r}(s)+a_2\Delta v(s)+a_3\Delta\theta(s). \tag{A13}$$

Among them, $\alpha_3=\frac{\theta_0}{C_{\rm P0}}\frac{\partial C_{\rm p}}{\partial\theta}$.

Paddle-variator control model normalization:

$$\Delta\theta(s)=b_1\Delta\omega_{\rm f}(s)+b_2. \tag{A14}$$

Among them, $b_1=k_{\rm p}\omega_{\rm f0}/\theta_0$, $b_2=k_{\rm i}t_{\rm s}\left(w_{\rm f0}-w_{\rm grated}\right)/\theta_0$.

Unitarization of Equation (10):

$$\Delta T_{\rm gref\_A}\,(s)=a_{10}\Delta\omega_{\rm f}(s)-a_{11}\Delta f(s). \tag{A15}$$

Among them, $a_{10}=-P_{\rm dem0}(1-\gamma)/\omega_{\rm f0}T_{\rm gref0}$, $a_{11}=k_{\rm PFKY}/T_{\rm grefN}$, similarly, $k_{\rm PFR}$ is used to replace $a_{11}$.

## Appendix B

$$G_{\mathrm{T}}(s)=\left(-\frac{B\cdot K_{\mathrm{TBs}}}{s}-\frac{1}{R_{\mathrm{T}}}\right)\frac{1}{T_{\mathrm{TC}}s+1}\frac{1}{T_{\mathrm{TT}}s+1}, \tag{A16}$$

$$G_{H}(s)=\left(-\frac{B\cdot K_{\mathrm{HBs}}}{s}-\frac{1}{R_{H}}\right)\frac{1}{T_{\mathrm{HT1}}s+1}\times\frac{1+T_{\mathrm{HR1}}s}{1+\left(\frac{R_{\mathrm{HT1}}}{R_{\mathrm{HP1}}}\right)T_{\mathrm{HR1}}s}\frac{1-T_{\mathrm{HW1}}s}{1+0.5T_{\mathrm{HW1}}s}, \tag{A17}$$

$$G_{\mathrm{ln}}(s)=\frac{1}{2H_{\mathrm{eq}}s+D_{\mathrm{eq}}}. \tag{A18}$$

## Appendix C

$$\frac{\Delta\omega_{\mathrm{g\_B}}(s)}{\Delta f(s)}=\frac{-k_{\mathrm{PFR}}\mu_{38}}{1-\frac{\mu_{34}\mu_{43}}{\left(1-\frac{\mu_{42}\mu_{24}}{(1-\mu_{21}\mu_{12})}\right)}}\frac{\mu_{87}\left(\mu_{87}\mu_{65}\mu_{53}+\mu_{87}\mu_{53}+\mu_{83}\right)}{1-\frac{\mu_{38}}{1-\frac{\mu_{34}\mu_{43}}{\left(1-\frac{\mu_{42}\mu_{24}}{(1-\mu_{21}\mu_{12})}\right)}}}, \tag{A19}$$

$$\frac{\Delta\omega_{\mathrm{g\_A}}(s)}{\Delta f(s)}=\frac{-k_{\mathrm{PFR}}\kappa_{38}}{1-\kappa_{34}\left(\frac{\kappa_{42}(\kappa_{21}\kappa_{19}\kappa_{95}\kappa_{53}+\kappa_{24}\kappa_{43})}{1-(\kappa_{21}\kappa_{12}+\kappa_{24}\kappa_{42})}+\kappa_{43}\right)}\frac{\kappa_{87}\left(\kappa_{87}\kappa_{65}\kappa_{53}+\kappa_{87}\kappa_{53}+\kappa_{83}\right)}{1-\frac{\kappa_{38}}{1-\kappa_{34}\left(\frac{\kappa_{42}(\kappa_{21}\kappa_{19}\kappa_{95}\kappa_{53}+\kappa_{24}\kappa_{43})}{1-(\kappa_{21}\kappa_{12}+\kappa_{24}\kappa_{42})}+\kappa_{43}\right)}}. \tag{A20}$$

## Appendix D

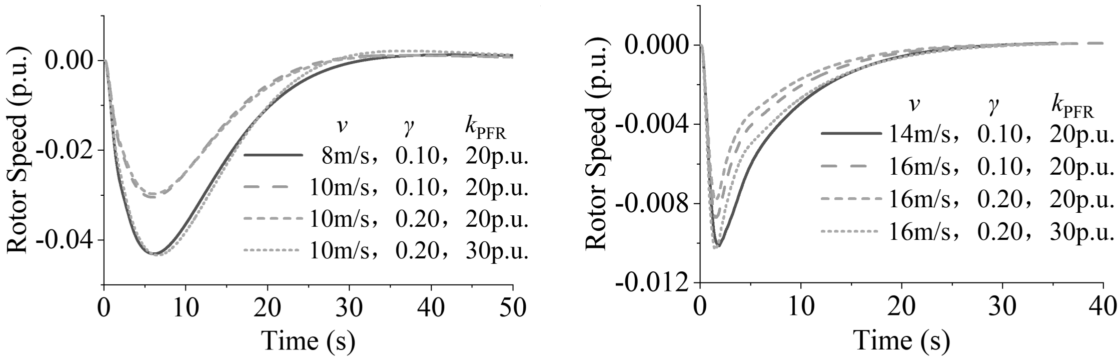


**(a)** Below rated wind speed

**(b)** Above rated wind speed

**Figure A1.** The rotor speed based on the step response.

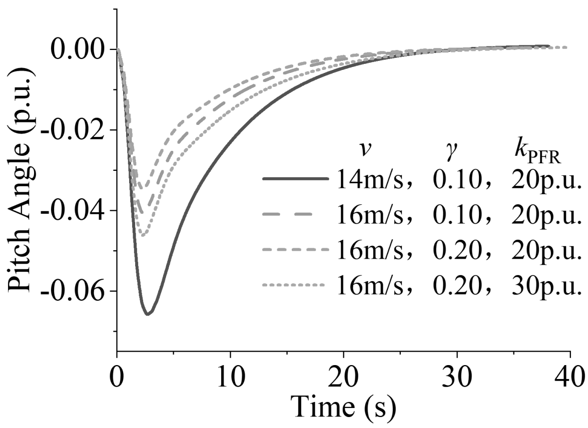


**Figure A2.** The pitch angle based on the step response.

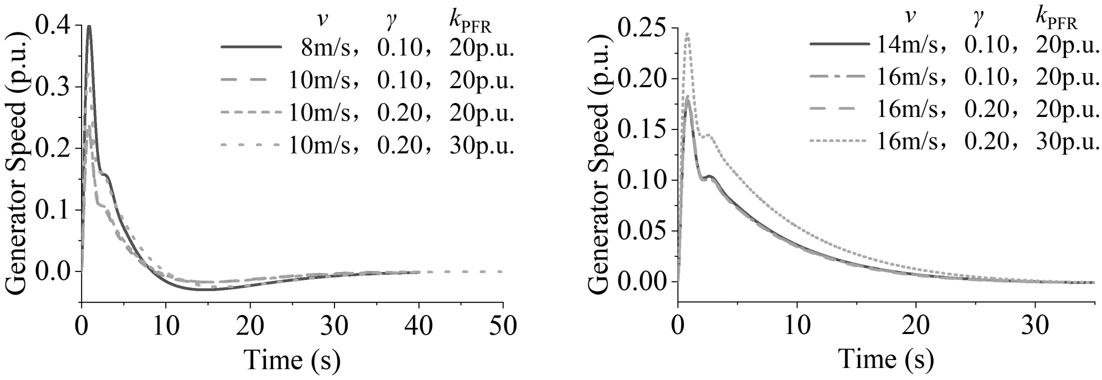


**(a)** Below rated wind speed **(b)** Above rated wind speed

**Figure A3.** The generator speed based on the step response.